

Strain-Induced Spin-Resonance Shifts in Silicon Devices

J. J. Pla,¹ A. Bienfait,² G. Pica,^{3,4} J. Mansir,⁵ F. A. Mohiyaddin,^{1,*} Z. Zeng,⁶ Y. M. Niquet,⁶
A. Morello,¹ T. Schenkel,⁷ J. J. L. Morton,⁵ and P. Bertet²

¹*School of Electrical Engineering and Telecommunications, University of New South Wales,
Anzac Parade, Sydney, New South Wales 2052, Australia*

²*Quantronics Group, SPEC, CEA, CNRS, Université Paris-Saclay,
CEA Saclay, 91191 Gif-sur-Yvette, France*

³*Center for Neuroscience and Cognitive Systems @UniTn,
Istituto Italiano di Tecnologia, Corso Bettini 31, 38068 Rovereto, Italy*

⁴*SUPA, School of Physics and Astronomy, University of St. Andrews,
St. Andrews KY16 9SS, United Kingdom*

⁵*London Centre for Nanotechnology, University College London,
17-19 Gordon Street, London WC1H 0AH, United Kingdom*

⁶*Université Grenoble Alpes, CEA, INAC-MEM, L_Sim, F-38000 Grenoble, France*

⁷*Accelerator Technology and Applied Physics Division, Lawrence Berkeley National Laboratory,
Berkeley, California 94720, USA*



(Received 26 August 2016; revised manuscript received 27 December 2017; published 10 April 2018)

In spin-based quantum-information-processing devices, the presence of control and detection circuitry can change the local environment of a spin by introducing strain and electric fields, altering its resonant frequencies. These resonance shifts can be large compared to intrinsic spin linewidths, and it is therefore important to study, understand, and model such effects in order to better predict device performance. We investigate a sample of bismuth donor spins implanted in a silicon chip, on top of which a superconducting aluminum microresonator is fabricated. The on-chip resonator provides two functions: it produces local strain in the silicon due to the larger thermal contraction of the aluminum, and it enables sensitive electron spin-resonance spectroscopy of donors close to the surface that experience this strain. Through finite-element strain simulations, we are able to reconstruct key features of our experiments, including the electron spin-resonance spectra. Our results are consistent with a recently observed mechanism for producing shifts of the hyperfine interaction for donors in silicon, which is linear with the hydrostatic component of an applied strain.

DOI: [10.1103/PhysRevApplied.9.044014](https://doi.org/10.1103/PhysRevApplied.9.044014)

I. INTRODUCTION

The spins of dopant atoms in silicon devices have been shown to exhibit great promise for quantum-information processing (QIP) [1–6]. The interest in this system has, in part, been motivated by the extraordinarily long spin-coherence times demonstrated, surpassing 1 s for the electron spin [7] and 3 h for the nuclear spin [8] of the phosphorus (³¹P) donor. Another group-V donor with considerable promise for QIP in silicon is bismuth (²⁰⁹Bi). Its large nuclear spin $I = 9/2$ and hyperfine constant $A = 1475$ MHz (which describes the interaction between the electron \mathbf{S} and nuclear \mathbf{I} spins $\mathbf{AS} \cdot \mathbf{I}$) provide rich features such as decoherence-suppressing atomic-clock transitions [9–11], where coherence times can exceed by 2 orders of magnitude those typically achieved using

other donor species. The Si:Bi system also possesses a large zero-field splitting of 7.375 GHz, making it an attractive dopant for use in hybrid superconducting devices [12,13] such as quantum memories [14–17].

In donor-based QIP devices, such as quantum bits and hybrid quantum memories, the donors are located within close proximity of control and detection circuitry on the surface of the silicon chip. Recent experiments on individual donor electron and nuclear spin qubits adjacent to nanoelectronic circuits [18] have highlighted the importance of considering the effect of these structures on the local environment of the spin. For example, it was shown that the spin-resonance frequencies of ³¹P donors in nanoelectronic devices can experience shifts from their bulklike values up to 4 orders of magnitude greater than their intrinsic linewidths [5,19–21]. These shifts have been attributed to strain and electric fields produced by surface metallic gates in the devices.

*Present Address: Quantum Computing Institute, Oak Ridge National Laboratory, Oak Ridge, Tennessee 37830, USA.

Strain is an inherent feature of MOS electronic devices, which often combine materials that have vastly different coefficients of thermal expansion (CTEs) [22,23]. It is, therefore, crucial to understand and predict the effect of intrinsic device strains on donors, as doing so can aid the design of scalable donor-based QIP and hybrid superconducting device architectures, serving as a guide to the often expensive and time-consuming fabrication process. Here, we study a sample of bismuth (^{209}Bi) donors implanted from 50 to 150 nm beneath a thin-film aluminum wire [Figs. 1(a) and 1(b)]. We observe the Si:Bi spin-resonance spectra in the device to be substantially altered from what is typically found in bulk experiments [10,24]. Through analyzing a range of mechanisms, we conclude that strain induced by differential thermal contraction of the silicon and the surface aluminum structure is the most likely explanation for the nontrivial spectra. A model is developed that is able to reproduce many facets of our measurements, demonstrating the ability to predict device behavior and illustrating the importance of considering strain in semiconductor micro- and nanoelectronic quantum devices.

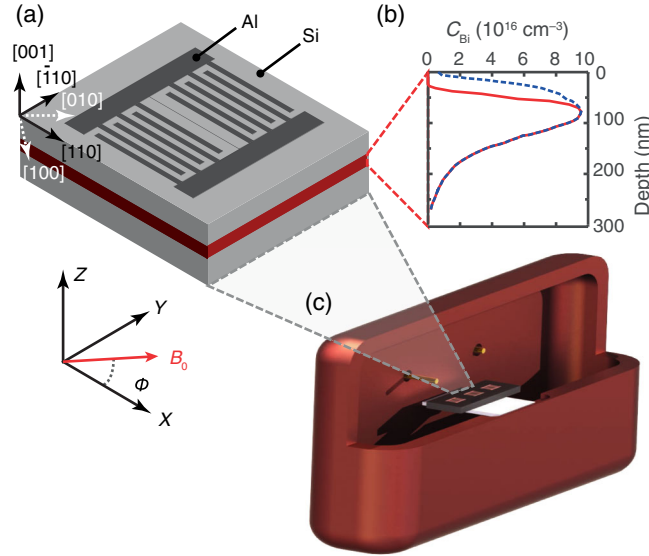


FIG. 1. (a) Sketch of an LC superconducting resonator made from a 50-nm-thick film of aluminum, patterned on a silicon substrate, with central inductor $5\ \mu\text{m}$ wide and $700\ \mu\text{m}$ long. While we show only one resonator here, there are three (almost identical) resonators patterned on the same chip [see (c)]. The silicon sample is cleaved along the $\langle 110 \rangle$ crystal axes, and we specify a sample frame such that $X \parallel [110]$, $Y \parallel [\bar{1}10]$, and $Z \parallel [001]$. The static field B_0 is oriented in the X - Y plane at a variable angle ϕ to X . (b) Bismuth donor doping profile. The blue dashed curve shows the result of a secondary-ion mass spectrometry (SIMS) measurement, while the red curve is the concentration of neutral donors obtained from a finite-element simulation performed using the SIMS profile that takes into account donor ionization from the Schottky junction between aluminum and silicon (see Sec. IV A). (c) Three-dimensional copper microwave cavity sample holder. The silicon chip is mounted on a sapphire holder (pictured in white) and is probed via the cavity input and output antennas.

The article is organized as follows: In Sec. II, we present the device architecture, physical system, and experimental setup utilized in our paper. Section III examines the electron spin-resonance spectra of bismuth donors beneath an aluminum wire, revealing nonbulklike splittings of the resonance peaks. Potential mechanisms behind the splittings are discussed in Sec. IV, and simulations of the spin-resonance spectra are performed in Sec. V for one of the mechanisms identified. We conclude by discussing the implications of the simulations and the broader significance of our results for QIP in Sec. VI.

II. EXPERIMENTAL DETAILS

A. Device

Our device [Fig. 1(a)] consists of three superconducting aluminum microwave resonators patterned on the surface of the same silicon chip via electron-beam lithography. The top 700 nm of silicon is an epitaxial layer of isotopically enriched 99.95% ^{28}Si , grown on an approximately 350- μm -thick high-resistivity float-zone silicon (100) wafer. The epitaxial layer is implanted with ^{209}Bi donors according to the profile depicted in Fig. 1(b).

The resonators are a lumped-element LC design. They contain a central inductive wire that produces an oscillating microwave magnetic field B_1 to drive and detect the spin resonance. The drive field B_1 is proportional to the magnetic vacuum fluctuations δB_1 in the resonator, a quantity that we can simulate directly for our device. We utilize δB_1 in the following calculations and discussion: it is readily determined from our simulations (unlike B_1 , which requires an accurate calibration of losses and other experimental parameters), and it provides us with another important measure, the spin-resonator coupling strength g . A simulation of δB_1 is performed knowing only the impedance of the resonator Z_0 and its frequency $\omega_0/2\pi$, and by calculating the resulting vacuum current fluctuations $\delta i = \omega_0 \sqrt{\hbar/(2Z_0)}$ in the wire (where \hbar is the reduced Planck's constant). The current-density distribution in the superconducting film [depicted in Fig. 2(a)] is evaluated using dc equations adapted from Ref. [25], which are valid for the calculation of our microwave current due to the negligible Ohmic losses at millikelvin temperatures and because the typical resonator frequency (about 7 GHz) is significantly smaller than the superconducting gap of aluminum [$2\Delta(0) \approx 140\ \text{GHz}$] [26]. The current-density distribution is then fed to a finite-element magnetostatic solver (COMSOL Multiphysics), with the resulting $|\delta B_1|$ profile shown in Fig. 2(b).

We observe a strong spatial dependence of the δB_1 orientation at the donor implantation depth [Fig. 2(c)]. Underneath the wire, the Y component of the field δB_{1Y} dominates, while, to the side, δB_{1Z} is the largest. We utilize this trait later in order to study spins in different spatial regions through orientation-dependent electron spin-resonance (ESR) spectroscopy [12,27].

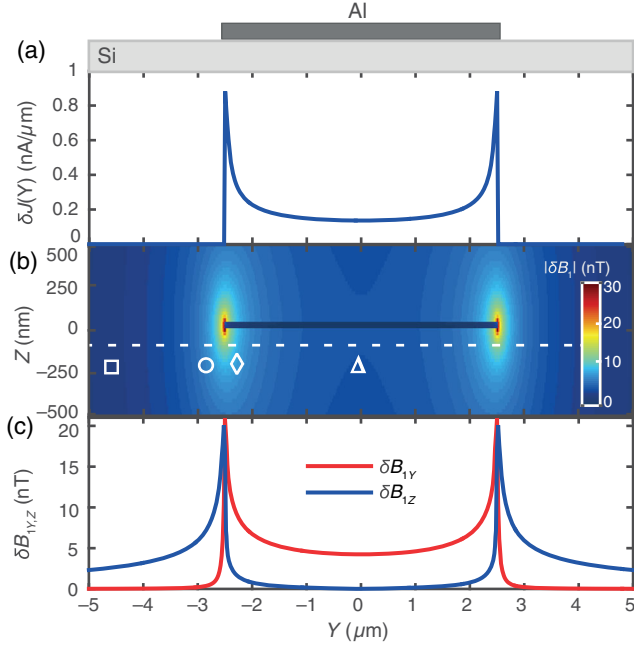


FIG. 2. (a) Calculation of the current-density vacuum fluctuations in the inductor. Equations describing the current-density profile are adapted from Ref. [25]. The only inputs to this calculation are the impedance of the resonator $Z_0 = 44 \Omega$ and its frequency $\omega_0/2\pi \approx 7.3$ GHz, extracted using CST Microwave Studio. (b) A COMSOL Multiphysics finite-element simulation of the spatial dependence of the magnetic-field vacuum fluctuation δB_1 magnitude produced by the current density in (a). The symbols beneath the white dashed line identify regions that will be referred to in the following sections. (c) Components of δB_1 along the Y and Z axes at a depth of 75 nm (corresponding to the peak donor concentration), marked by the white dashed line in (b).

B. Physical system

At cryogenic temperatures, the bismuth donors bind an additional valence electron compared to the silicon atoms of the host crystal, providing a coupled electron ($S = 1/2$) and nuclear ($I = 9/2$) spin system that is described by the Hamiltonian

$$H_0/h = \gamma_e \mathbf{B}_0 \cdot \mathbf{S} - \gamma_n \mathbf{B}_0 \cdot \mathbf{I} + A \mathbf{S} \cdot \mathbf{I}, \quad (1)$$

where $\gamma_e = 28$ GHz/T ($\gamma_n = 6.963$ MHz/T) is the electron (nuclear) gyromagnetic ratio and B_0 is a static magnetic field applied in the plane of the aluminum resonators—with a variable angle ϕ relative to the inductive wire [see Fig. 1(a)]—that allows us to fine-tune the spin transition frequencies of the ^{209}Bi donors.

At values of the magnetic field where the electron Zeeman frequency $E_z/h = \gamma_e B_0 \lesssim A$, the eigenstates become strongly mixed in the electron-nuclear spin basis and are best described by the total spin $\mathbf{F} = \mathbf{I} + \mathbf{S}$ and its projection onto B_0 , m_F [9]. We choose the frequencies of the resonators to be close to the Si:Bi zero-field splitting of 7.375 GHz in order to minimize field-induced losses in the superconducting films, achieving $\omega_{0A}/2\pi = 7.305$ GHz for resonator A, $\omega_{0B}/2\pi = 7.246$ GHz for resonator B and $\omega_{0C}/2\pi = 7.144$ GHz for resonator C. We therefore operate in the regime where F and m_F are good quantum numbers and we describe states in the $|F, m_F\rangle$ basis. In the following analysis and discussion, we focus on resonators A and B—those with frequencies closer to the zero-field splitting, which we are able to study the most extensively. Table I presents important parameters that characterize the

TABLE I. Numerical calculations of the spin transition parameters for the Si:Bi system at the LC resonator frequencies listed. Parameters include the resonance field (B_0), the transition matrix element ($M = |\langle F, m_F | S_X | F', m'_F \rangle|$, $|\langle F, m_F | S_Z | F', m'_F \rangle|$ for the $|\Delta F \Delta m_F| = 1, 0$ transitions; see Appendix A), and the transition frequency sensitivity to the magnetic field (df/dB_0), the electron g factor (df/dg), the hyperfine interaction (df/dA), and the quadrupole interaction (df/dQ).

| Resonator A, $\omega_{0A}/2\pi = 7.305$ GHz | | | | | | | |
|---|-----------------------|------------|------|----------------------|---------|---------------|---------|
| Transition | $\Delta F \Delta m_F$ | B_0 (mT) | M | $(df/dB_0)/\gamma_e$ | df/dA | df/dg (MHz) | df/dQ |
| 1A: $ 4, -4\rangle \leftrightarrow 5, -5\rangle$ | -1 | 2.86 | 0.47 | -0.90 | 5.00 | -36.0 | 2.45 |
| 2A: $ 4, -4\rangle \leftrightarrow 5, -4\rangle$ | 0 | 3.22 | 0.30 | -0.80 | 5.00 | -35.9 | -19.1 |
| 3A: $ 4, -4\rangle \leftrightarrow 5, -3\rangle$ | 1 | 3.69 | 0.07 | -0.69 | 5.00 | -35.8 | -35.9 |
| 4A: $ 4, -3\rangle \leftrightarrow 5, -4\rangle$ | -1 | 3.69 | 0.42 | -0.69 | 5.00 | -35.8 | 6.14 |
| 5A: $ 4, -3\rangle \leftrightarrow 5, -3\rangle$ | 0 | 4.32 | 0.40 | -0.59 | 5.00 | -35.7 | -10.6 |
| 6A: $ 4, -3\rangle \leftrightarrow 5, -2\rangle$ | 1 | 5.22 | 0.13 | -0.49 | 5.00 | -35.4 | -22.6 |
| 7A: $ 4, -2\rangle \leftrightarrow 5, -3\rangle$ | -1 | 5.22 | 0.37 | -0.49 | 5.00 | -35.5 | 7.42 |
| 8A: $ 4, -2\rangle \leftrightarrow 5, -2\rangle$ | 0 | 6.60 | 0.46 | -0.38 | 5.00 | -35.0 | -4.54 |
| Resonator B, $\omega_{0B}/2\pi = 7.246$ GHz | | | | | | | |
| Transition | $\Delta F \Delta m_F$ | B_0 (mT) | M | $(df/dB_0)/\gamma_e$ | df/dA | df/dg (MHz) | df/dQ |
| 1B: $ 4, -4\rangle \leftrightarrow 5, -5\rangle$ | -1 | 5.20 | 0.47 | -0.90 | 5.00 | -65.4 | 2.49 |
| 2B: $ 4, -4\rangle \leftrightarrow 5, -4\rangle$ | 0 | 5.88 | 0.31 | -0.79 | 5.00 | -65.1 | -19.0 |
| 3B: $ 4, -4\rangle \leftrightarrow 5, -3\rangle$ | 1 | 6.74 | 0.07 | -0.69 | 5.00 | -64.8 | -35.7 |
| 4B: $ 4, -3\rangle \leftrightarrow 5, -4\rangle$ | -1 | 6.75 | 0.42 | -0.69 | 5.00 | -64.9 | 6.27 |

low-field ($B_0 < 7$ mT) spin-resonance transitions that are probed in our experiments.

C. Sample mounting

The device is fixed to a sapphire wafer with a small amount of vacuum grease (which serves to minimize the sample strains produced through mounting), and the sapphire is then clamped between the halves of a rectangular copper microwave cavity [Fig. 1(c)], which acts as a sample enclosure and permits high quality factors for the superconducting resonators by suppressing radiation losses. The copper cavity is attached to the cold finger of a dilution refrigerator and cooled to a base temperature of 20 mK, where we are able to detect the spin-echo signals produced by the small number of shallow-implanted donors underneath each wire (estimated at approximately 10^7) by utilizing a quantum-noise-limited ESR setup, as described in Refs. [12,28,29]. We direct the reader to the Supplemental Material of Ref. [12] for a full schematic of the experimental setup.

III. SPIN-RESONANCE SPECTRA

A. Echo-detected field sweep

In this section, we provide a detailed discussion of the Si:Bi ESR spectra, first reported in Refs. [12,13]. We observe the ESR spectrum for resonator *B* by performing an echo-detected magnetic-field sweep on the lowest-field spin-resonance line [indicated by the arrow in Fig. 3(a)], corresponding to transition 1*B*, i.e., between the states $|4, -4\rangle \leftrightarrow |5, -5\rangle$ (see Table I). We integrate the echo signal A_e from a Hahn echo sequence [30] [over the dashed region depicted in the pulse protocol of Fig. 3(b)] and step the magnetic field B_0 . The sweep is first performed with $B_0 \parallel X$ ($\phi = 0^\circ$), then repeated with the orthogonal orientation $B_0 \parallel Y$ ($\phi = 90^\circ$); the resulting traces are shown in Fig. 3(c). The doped silicon sample investigated in this paper has also been characterized using a standard “bulk” ESR spectrometer at the X band and with no planar on-chip resonator [24]. The gray solid curve in Fig. 3(c) represents the spin-resonance spectrum from this work extrapolated to the spin transition and frequency utilized in our experiment (see Appendix B for further details). Instead of measuring a single peak with a linewidth of approximately 20 μT (as expected from the X-band measurement), we observe that the resonance is split into two peaks. Each peak has a linewidth of about 100 μT , representing a total broadening of more than an order of magnitude.

Varying the amplitude of the refocusing π pulse in the echo sequence reveals a series of Rabi oscillations (A_e is maximized whenever the refocusing pulse equals an odd multiple of π), and the frequency of these oscillations is observed to depend strongly on the magnetic field B_0 [Fig. 3(b)] across these two peaks. The traces in Fig. 3(c) are recorded in a “Rabi-levelled” manner, ensuring that, at

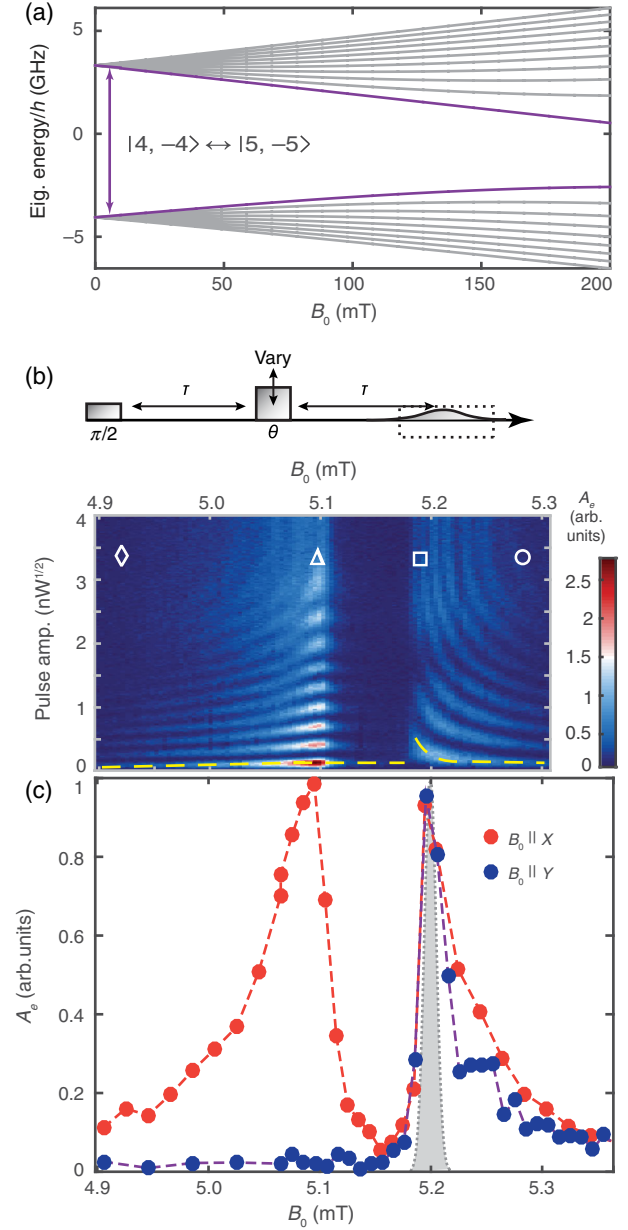


FIG. 3. (a) Eigenstate frequencies of the Si:Bi system. The purple states and arrow identify the $|4, -4\rangle \leftrightarrow |5, -5\rangle$ transition (1*B*) probed in (b) and (c). (b) Rabi oscillations as a function of B_0 for transition 1*B*. The amplitude of the refocusing pulse in a Hahn echo sequence (shown above) is varied to reveal oscillations in the integrated echo signal A_e (marked with a black dashed box in the sequence). Symbols identify spectral regions produced by spins at specific locations in the device [see Fig. 2(b)]. (c) A Rabi-levelled echo-detected field sweep, taken using the calibrated π -pulse amplitudes of (b) (the yellow dashed line). The gray-filled curve depicts the expected ESR spectrum, while the solid circles show the measured spectra (averaged over eight sequences with a repetition rate of 0.2 Hz) for different field orientations. A 2% correction is applied to B_0 for the measured data (within the magnet calibration error) so that the high-field peak aligns with the theoretical transition field. The same correction is applied to all of the experimental data in this work.

each value of B_0 , the pulse amplitude is chosen to provide well-calibrated π and $\pi/2$ pulses [the yellow dashed line in Fig. 3(b)].

The nontrivial peak splitting and field dependence of the Rabi frequency observed in Figs. 3(b) and 3(c) can be understood by examining the experimental details, starting with the relevant bandwidths of the echo sequence. The $\pi/2$ pulse of the Hahn echo readout provides the initial excitation of spins that contribute to the echo signal. It has a duration of $t_{\pi/2} = 2.5 \mu\text{s}$ and an excitation bandwidth of approximately 500 kHz. This pulse is heavily filtered by the resonator, reducing its bandwidth to a value determined by the resonator linewidth $\kappa = \omega_0/Q \approx 2\pi \times 25 \text{ kHz}$ (where $Q = 3.2 \times 10^5$ is the quality factor of resonator B). Thus, only spins with resonant frequencies that lie inside the resonator bandwidth contribute to the measurement. In addition, these spins experience a relaxation rate which is 3 orders of magnitude greater than the intrinsic value due to the Purcell effect [13]. This enhanced relaxation is suppressed quadratically with the spin-resonator frequency detuning, such that off-resonant spins display substantially longer energy relaxation times T_1 and quickly become saturated under the 0.2-Hz repetition rate of the experiment. Each B_0 in Figs. 3(b) and 3(c), therefore, corresponds to a highly selective measurement on a small subensemble of spins with a resolution $\Delta B = \kappa/(df/dB_0) = 1 \mu\text{T}$, where df/dB_0 is the transition frequency field sensitivity (listed in Table I).

Comparing the echo-detected spectra for the different orientations of B_0 [the red and blue circles in Fig. 3(c)] provides strong evidence that the splitting and inhomogeneous broadening of the ESR transition results from the presence of the on-chip LC resonator. We find that the low-field peak vanishes for $B_0 \parallel Y$ ($\phi = 90^\circ$), while the high-field peak remains relatively unchanged. This disappearance can be understood by referring to Fig. 2(c) and noting that the spin transition probed here ($1B$; see Table I) obeys the selection rule $|\Delta m_F| = 1$ and is therefore excited only when $\delta B_1 \perp B_0$. For $B_0 \parallel Y$, the condition $\delta B_1 \perp B_0$ is met only for spins to the side of the wire (which experience a δB_1 field along Z). Spins underneath the wire (where the δB_1 field is almost entirely along Y) are not measured in this scan. For the spectrum recorded with $B_0 \parallel X$ ($\phi = 0^\circ$), spins underneath the wire as well as those to the side observe $B_0 \perp \delta B_1$ and thus contribute to the echo signal. Thus, the low-field (vanishing) peak likely corresponds to the spins below the wire, while the high-field peak is produced by spins to its side, indicating that the presence of the inductive wire is the source of the splitting. In Sec. IV, we discuss a number of potential mechanisms (e.g., an in-built electric field, a Meissner-induced magnetic-field inhomogeneity, and strain) through which this splitting could occur. The spin-resonance frequency of the donors therefore depends on their location relative to the wire. By measuring only a small fraction of the large

inhomogeneously broadened transition at each B_0 field ($1 \mu\text{T}$ against approximately $200 \mu\text{T}$) in Fig. 3(c), we are effectively probing subensembles of donors residing in specific locations in the device.

We now return to the B_0 dependence of the Rabi oscillations [Fig. 3(b)] and demonstrate that the picture described above is in good agreement with these data. The coupling strength between each spin and the resonator is given by $g = \gamma_e M |\delta B_{1\perp}|$, where M is the ESR transition matrix element (see Table I) and $|\delta B_{1\perp}|$ is the magnitude of the δB_1 component felt by the spin that is perpendicular to B_0 . The Rabi frequency Ω_R then has a linear dependence on the δB_1 field through the relation $\Omega_R = 2g\sqrt{\bar{n}}$, where \bar{n} is the mean intracavity photon number (proportional to the input microwave power). For the high-field peak in the ESR spectra (originating from spins located to the side of the wire), the sharp transition at the low-field edge likely corresponds to spins far from the wire that are bulklike in their behavior. Being far from the wire, these spins also experience a reduced δB_1 value [see Fig. 2(c)] and thus Rabi frequency, observed as longer-period oscillations in Fig. 3(b). Moving closer to the wire increases the spin-resonance shifts (i.e., through larger electric or strain fields), as well as the magnitude of the δB_1 field felt by the spins. We thus anticipate that the tail regions of the lines will have an enhanced Rabi frequency, and this is indeed the case. The symbols overlaid on Fig. 3(b) summarize the above discussion by correlating the different spectral regions with spins from specific locations in the device [see the corresponding symbols in Fig. 2(b)].

B. Extended spectra

To help identify the mechanism behind the wire-induced peak splitting and broadening, we probe additional spin-resonance transitions (listed in Table I) using resonators A and B, which display different sensitivities to the various Hamiltonian parameters. In Fig. 4(a), we plot the calculated low-field ESR transition frequencies and their crossing with resonator A. Transitions obeying the usual spin selection rule $\Delta m_F = \pm 1$ (the solid lines) are accessed in the experiment by ensuring that $B_0 \perp \delta B_1$, as is the case for the previous measurement on transition $1B$. Such transitions are typically referred to as being of the “ S_X ” type since it is primarily the S_X operator that drives spin flips between the states. Transitions obeying the selection rule $\Delta m_F = 0$ [the dashed lines in Fig. 4(a)]—of the so-called S_Z type—are probed in the experiment with the alignment $B_0 \parallel \delta B_1$ (i.e., $B_0 \parallel Y$). We refer the reader to Appendix A for a detailed discussion of these two types of spin-resonance transitions.

A measurement of the first transitions with $B_0 \parallel X$ ($\Delta m_F = \pm 1$) is shown in the Rabi-levelled echo-detected field sweep of Fig. 4(b) (the red trace) for resonator A. Also presented here is the spectrum recorded with $B_0 \parallel Y$ (the blue trace), which is composed of both $\Delta m_F = 0$

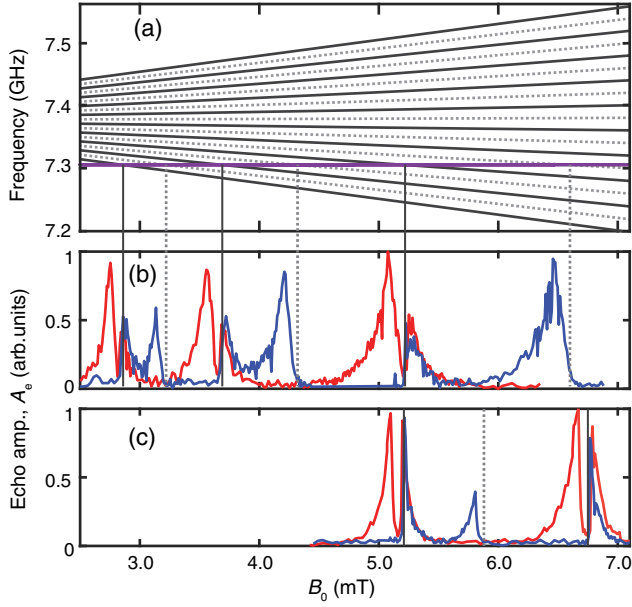


FIG. 4. (a) ESR transition frequencies of the Si:Bi system for $B_0 < 7$ mT. The solid lines represent the spin transitions that obey the selection rule $\Delta m_F = \pm 1$ (i.e., $\delta B_1 \perp B_0$), while the dashed lines show $\Delta m_F = 0$ transitions ($\delta B_1 \parallel B_0$). The purple solid line indicates the frequency of resonator A ($\omega_{0A}/2\pi = 7.305$ GHz). Rabi-levelled echo-detected field sweeps of the ESR transitions below 7 mT of (b) resonator A and (c) resonator B. The theoretical spin transition frequencies are identified by the gray solid and dashed lines.

resonances from spins underneath the wire (where $B_0 \parallel \delta B_1$) and $\Delta m_F = \pm 1$ resonances from spins to the side of the wire (where $B_0 \perp \delta B_1$). The $\Delta m_F = 0$ transitions are observed to lack a splitting; this is further evidence that they originate from spins located predominantly underneath the wire (the only region with $B_0 \parallel Y$). The

TABLE II. Experimental center fields (B_{0c}) and peak splittings (ΔB_0) extracted from the measured ESR transitions for resonators A and B. $\Delta F \Delta m_F = 0$ transitions do not display a splitting and are therefore not included. Although the $\Delta F \Delta m_F = \pm 1$ transitions are almost degenerate here, we attribute the peaks to the $\Delta F \Delta m_F = -1$ transitions, which exhibit larger transition matrix elements M . We do not attempt to extract linewidths of the peaks due to their highly asymmetrical shapes.

| Resonator A, $\omega_{0A}/2\pi = 7.305$ GHz | | |
|---|---------------|-------------------|
| Transition | B_{0c} (mT) | ΔB_0 (mT) |
| 1A | 2.87 | 0.11 |
| 4A | 3.71 | 0.15 |
| 7A | 5.28 | 0.20 |
| Resonator B, $\omega_{0B}/2\pi = 7.246$ GHz | | |
| Transition | B_{0c} (mT) | ΔB_0 (mT) |
| 1B | 5.24 | 0.11 |
| 4B | 6.84 | 0.14 |

experiments are repeated for resonator B and displayed in the lower traces of Fig. 4(c). We list the extracted peak splittings of the recorded transitions in Table II.

IV. PEAK SPLITTING MECHANISMS

We now turn to the analysis of possible mechanisms through which the presence of the aluminum wire may induce a splitting and broadening of the observed ESR spectra.

A. Built-in voltage

The aluminum-silicon interface formed beneath the resonator constitutes a Schottky junction. Band bending at the interface results from the difference in work functions of the aluminum and silicon (or from Fermi-level pinning to surface states) [31]. The band bending causes the ionization of bismuth donors within an area known as the depletion region. Donor ionization continues into the semiconductor until a sufficient space charge has been accumulated to counter the band bending. Immediately outside of the depletion region, the total electric field is reduced to zero. At finite temperatures, however, the edge of the depletion region is broadened according to Fermi-Dirac statistics, and a small fraction of neutral donors can experience large electric fields. Such donors would display a Stark shift of the hyperfine interaction [20] or electron g factor through

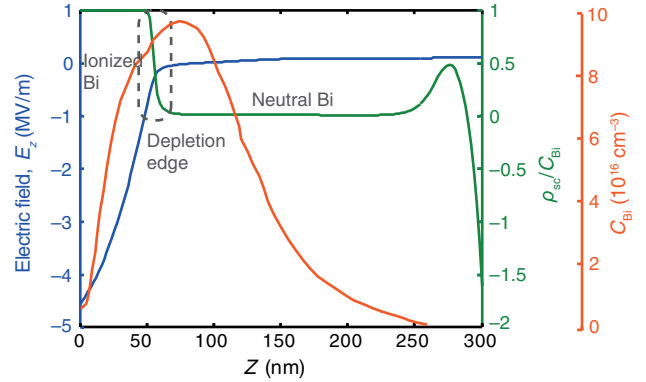


FIG. 5. Fraction of ionized donors, built-in electric field, and doping profile versus the depth beneath the aluminum resonator. The implanted Bi profile (as determined from a secondary-ion mass spectrometry measurement) is shown in orange. The green curve provides the space charge density ρ_{sc} (which represents the density of ionized donors) divided by the donor concentration C_{Bi} . Calculations are performed with the finite-element electrostatic solver ISE-TCAD, with a simulation temperature of 5 K (the minimum temperature at which convergence is achieved) and an assumed background boron doping density of 10^{13} cm $^{-3}$. The gray dashed box highlights the edge of the depletion region. This roll-off is expected to get steeper at the experimental temperature of 20 mK. At about a 275-nm depth, the bismuth donors are ionized once again (this time to the background boron acceptors present in the sample) before the space charge density becomes negative, indicating the presence of ionized boron dopants.

the electric field, altering their resonant frequencies from those to the side of the wire away from the depletion region.

We perform finite-element simulations with the commercial software ISE-TCAD, which solves the Poisson equation self-consistently to extract the electric fields and ionized bismuth concentration underneath the wire, the results of which are shown in Fig. 5. This plot demonstrates that the broadening of the depletion region edge is small relative to the width of the implantation profile, even at the elevated simulation temperature of 5 K—the minimum temperature at which convergence is achieved. Donors at depths of less than 50 nm are mostly ionized, while donors deeper than that are neutral and experience negligible electric fields (<50 kV/m, with expected Stark shifts below 1 kHz [32]). At the experimental temperature of 20 mK, we expect an even sharper depletion region boundary. We therefore discount this mechanism as the cause for the spectral broadening and remove the shallow donors (<50 nm) beneath the wire from the spectra simulations in the following sections.

B. Magnetic-field inhomogeneity

It is conceivable that the superconducting resonator could perturb the static magnetic field in a manner that produces differing magnetic-field profiles beneath the wire and to its side. For example, this inhomogeneity might result from the component of a misaligned B_0 field perpendicular to the aluminum film, concentrating above or below the wire due to the Meissner effect [33]. The strength of any such inhomogeneity increases in proportion to the magnitude of B_0 and, as the resonators are fabricated within 2 mm of one another on the same silicon chip, the inhomogeneity would be nearly identical for each of the resonators. We can rule this mechanism out due to the fact that we observe the same splitting and linewidth of the first spin transition for resonators *A* and *B* (see Table II) and also *C* (see Appendix C), despite the transition for resonator *C* occurring at almost twice the field of resonator *B* and 3 times that of resonator *A*.

C. Strain

Strain can alter the spin transition frequencies of donors in silicon through several mechanisms. It has been shown that the nuclear-magnetic-resonance (NMR) frequencies of donors with nuclear spin $I > 1/2$ [34,35] (e.g., arsenic, antimony, and bismuth) can be shifted through a strain-induced quadrupole interaction (QI). Strain can also modify the hyperfine interaction strength A [36] or the electron g factor g_e , both of which result in shifts of the spin-resonance frequencies. Here, we analyze all three of these mechanisms (QI, A , and g_e) to determine if they are capable of accounting for the ESR spectra presented in Sec. III.

In order to aid in our discussion, we first explain the origin of strain in our device and provide an estimate of its magnitude and spatial distribution through simulations.

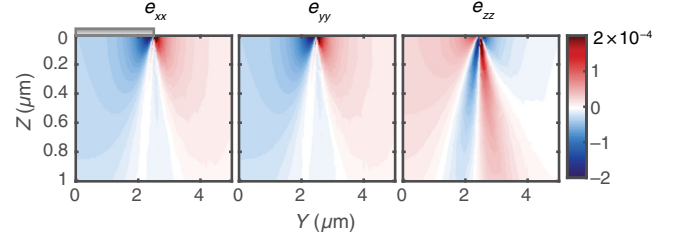


FIG. 6. Finite-element COMSOL simulations of the strain tensor components along the principle crystal axes $x||[100]$, $y||[010]$, and $z||[001]$ and their variation as a function of position in the device. A cross section of the aluminum wire (drawn to scale) is represented by the gray gradient-filled box above the silicon substrate (which bounds the strain data). Only half of the wire is displayed here due to it being symmetric about its center. Here, the xyz crystal axes are related to the sample frame XYZ (used to describe δB_1 and the orientation of B_0) by a 45° rotation about Z [see Fig. 1(a)]. We show the result for the wire running parallel to the $[110]$ (or X) axis, the direction in which the sample is cleaved.

The aluminum resonator is deposited on the silicon substrate by electron-beam evaporation at room temperature, where the device is assumed to be strain-free [37,38]. While the evaporation temperature may be above room temperature in practice, it is assumed to be only a fraction of the total temperature range explored in our experiments ($\Delta T \approx 300$ K). As the device is cooled to 20 mK, the approximate tenfold difference in the CTEs of silicon and aluminum produces substantial device strains through differential thermal contraction. We perform finite-element simulations of these strains using the software package COMSOL Multiphysics, where we include temperature-dependent CTEs of the materials [39–41] and the anisotropic stiffness coefficients for silicon [42]. Three of the six independent strain tensor components (those along the $\langle 100 \rangle$ crystal axes) are plotted in Fig. 6 as a function of position. The full strain tensor and its spatial dependence can be found in Appendix D.

1. Quadrupole interaction

There have been several recent studies that report on quadrupole interactions of group-V donors in silicon, generated by strain [34,35] or interface defects [43]. Nuclei with a spin $I > 1/2$ can have a nonspherical charge distribution and an associated quadrupole moment Q [44]. This charge distribution has an axis of symmetry that aligns with the nuclear angular momentum and interacts with an electric-field gradient (EFG) $V_{\alpha\beta}$ (where α and β are the principal axes in the local crystal coordinate system) produced by external charges, such as the donor-bound electron. The interaction is described by the following quadrupole Hamiltonian:

$$H_Q/h = \gamma \frac{eQV_{zz}}{4I(2I-1)h} [3I_z^2 - \mathbf{I}^2 + \eta(I_x^2 - I_y^2)], \quad (2)$$

where γ is a multiplicative scaling factor (resulting from the Sternheimer antishielding effect [44]), e is the electron charge, h is Planck's constant, \mathbf{I} is the nuclear spin operator with components I_α , I in the denominator is the scalar value of the nuclear spin ($I = 9/2$), and $\eta = (V_{xx} - V_{yy})/V_{zz}$ is an asymmetry parameter. It is evident from Eq. (2) that the existence of an EFG $V_{\alpha\beta}$ produces a frequency shift between states with different nuclear spin projections m_I . In the case of the Si:Bi spin system, quadrupole shifts in the ESR spectra are evident at low magnetic fields because the electron and nuclear spin states are strongly mixed by the hyperfine interaction.

In Table I, we list the sensitivities of the transitions to the quadrupole coefficient $Q_{zz} = \gamma e Q V_{zz} / [4I(2I - 1)h]$ (the prefactor in the quadrupole Hamiltonian H_Q). By comparing the sensitivities df/dQ to the extended ESR spectra (Fig. 4) and the observed peak splittings (Table II), it becomes apparent that the quadrupole interaction is unlikely to be the origin of the nontrivial spectra shape. The peak splittings ΔB_0 of different transitions for the same resonator approximately follows their magnetic-field sensitivities df/dB_0 (see Table I), implying an underlying mechanism with a constant frequency distribution across all transitions. This is clearly not the case for the quadrupole interaction, where df/dQ increases with the transition number. Furthermore, the $\Delta F \Delta m_F = 0$ transitions have sensitivities of opposite sign to the $\Delta F \Delta m_F = -1$ transitions—the asymmetry of this resonance is therefore expected to be the opposite of that of the low-field peak in the $\Delta F \Delta m_F = -1$ transition, as they both correspond to spins in the same region of the device (underneath the wire). However, this opposite symmetry is not apparent in Fig. 4.

Whereas df/dQ is strongly dependent on the transition, we note that df/dA is constant (see Table I), so a strain-induced inhomogeneous hyperfine interaction is likely to have the desired properties for the comparison of different transitions.

2. Hyperfine interaction

Silicon has a conduction-band minimum that is sixfold degenerate along the $\langle 100 \rangle$ equivalent crystallographic directions—commonly referred to as “valleys” [45]. The degeneracy of these valleys is broken by the confining potential of the donor, resulting in a singlet A_1 ground state and doublet E and triplet T_2 excited states [46]. For a donor in a bulk silicon crystal (in the absence of strain and electric fields), the electron is perfectly described by the singlet ground state $|\psi\rangle = |A_1\rangle$. The E and T_2 state wave functions have vanishing probabilities at the nucleus [i.e., $|\psi(0)|^2 = 0$] and, consequently, do not exhibit a hyperfine interaction ($A = 0$). Applying strain to a valley shifts its energy relative to the conduction-band minimum, resulting in a rearrangement of the relative populations of each valley which can be described as a mixing of the donor A_1 and E states. The degree of mixing can be calculated using the

“valley repopulation” model (VRM) [47], which predicts a quadratic shift of the hyperfine interaction with an applied strain [48]:

$$\frac{\Delta A(\epsilon)}{A(0)} = -\frac{\Xi_u^2}{9E_{12}^2}[(\epsilon_{xx} - \epsilon_{yy})^2 + (\epsilon_{xx} - \epsilon_{zz})^2 + (\epsilon_{yy} - \epsilon_{zz})^2], \quad (3)$$

where $\Xi_u \approx 8.7$ eV is the uniaxial deformation potential of silicon, E_{12} is the energy splitting between the A_1 and E states, and ϵ is a general strain tensor with principal components $\epsilon_{\alpha\alpha}$ (where α are the cubic axes $x||[100]$, $y||[010]$, and $z||[001]$). This expression is valid in the limit of a small ϵ ($|\epsilon_{\alpha\alpha}| \lesssim 1 \times 10^{-3}$) and is applicable to the range of strain produced in our device. In Fig. 7(a), we plot the hyperfine shift $\Delta A(\epsilon)$ close to the inductive wire, calculated using Eq. (3). The quadratic dependence of $A(\epsilon)$ on strain implies that it is only ever reduced from $A(0)$, the unstrained value. It is apparent that such a distribution could not explain the spectra of Sec. III, which would require both positive and negative frequency components in order to split the resonance peak in the manner observed. In addition, the VRM predicts $\Delta A \approx 100$ kHz for strains on the order of 10^{-4} , equating to a resonance shift of $\Delta A \times (df/dA)/(df/dB_0) = 20$ μ T, an order of magnitude smaller than our observed peak broadening.

Very recently, it was shown experimentally that the hyperfine interaction of donors in silicon is also sensitive to the hydrostatic component of strain [48]. This result is surprising, as the VRM predicts no hyperfine reduction for strains that shift all of the valleys by the same energy.

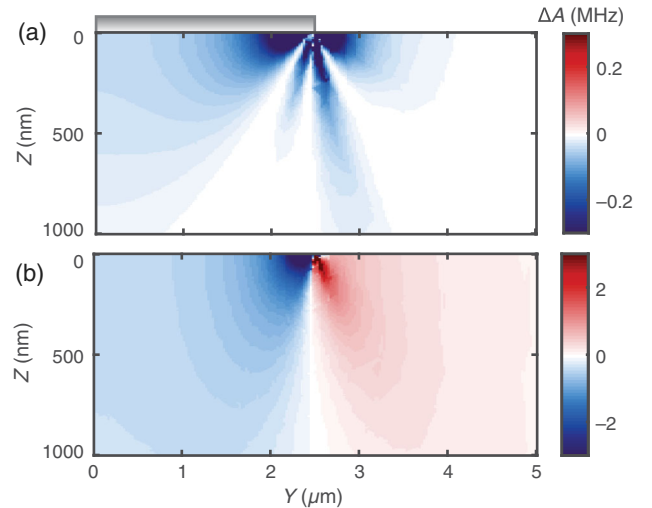


FIG. 7. Calculation of the hyperfine interaction reduction as a result of the simulated device strain. (a) Calculated hyperfine shift ΔA according to the valley repopulation model, which predicts a quadratic dependence on strain. (b) Calculation performed using the second-order strain model of Eq. (4). The second-order model predicts shifts an order of magnitude larger than the VRM does and also displays bipolar frequencies due to its strong linear dependence.

A second-order strain model for the hyperfine shift was proposed:

$$\frac{\Delta A(\epsilon)}{A(0)} = \frac{K}{3}(\epsilon_{xx} + \epsilon_{yy} + \epsilon_{zz}) + \frac{L}{2}[(\epsilon_{xx} - \epsilon_{yy})^2 + (\epsilon_{xx} - \epsilon_{zz})^2 + (\epsilon_{yy} - \epsilon_{zz})^2] + N(\epsilon_{xy}^2 + \epsilon_{xz}^2 + \epsilon_{yz}^2), \quad (4)$$

with $K = 29$, $L = -9064$, and $N = -225$ being the model coefficients for ^{209}Bi calculated using tight-binding theory and $K = 17.5$ extracted from a first-principles calculation using density-functional theory. Remarkably, for $|\epsilon| \lesssim 1 \times 10^{-3}$, the model predicts that the linear hydrostatic strain dominates the hyperfine shift. It is suggested that this term is due primarily to strain effects on the central-cell potential, inducing a coupling between the $1s A_1$ state and higher donor orbital states with the same symmetry. Experiments confirm that the existence of the linear term and the extracted coefficient $K = 19.1$ is in good agreement with theory. A calculation of the hyperfine shift distribution in the device using the full second-order strain model [Eq. (4)] is shown in Fig. 7(b). For strains on the order of 10^{-4} , we expect $\Delta A \approx 1$ MHz and an equivalent resonance shift of about $200 \mu\text{T}$. In addition, the sensitivity of the resonance frequency to the hyperfine interaction is constant across all spin transitions (see Table I), in agreement with the peak splittings extracted in Table II. This mechanism provides bipolar resonance shifts of the correct magnitude and thus constitutes a likely explanation for the spectra of Fig. 3(c). It should be noted that such a mechanism is not unique to bismuth, a linear hyperfine tuning with strain is observed for all of the group-V donors in silicon [48].

3. g factor

The final mechanism we consider is a strain-induced shift of the electron g factor g_e . Strain modifies g_e directly (by admixing higher-lying energy bands) and through the valley repopulation effect [47]. These two effects alter the gyromagnetic ratio $\gamma_e = g_e \mu_B / \hbar$ (where μ_B is the Bohr magneton), shifting the spin-resonance frequency through the electron Zeeman interaction $\gamma_e \mathbf{B}_0 \cdot \mathbf{S}$. The g -factor shift for donors in silicon has been predicted and measured to be several orders of magnitude smaller than that of the hyperfine interaction [47,49]. In addition, the electron Zeeman energy for the range of fields applied in our study ($B_0 < 7$ mT) is small, with $E_z / \hbar = \gamma_e B_0 < 300$ MHz, thus providing a proportionally lower contribution to the transition frequency than the hyperfine interaction $A = 1457$ MHz. We quantify the difference between these two effects with the transition parameter data in Table I. For the same relative change, the hyperfine interaction shifts the resonant frequency by a factor $(A \times df/dA) / (g_e \times df/dg)$ greater than does the electron g factor, which ranges from 50 to 100 for the spin transitions explored here. Finally, comparing the g -factor sensitivity df/dg for the transitions

of resonator A to those of resonator B , we expect the splittings and broadenings to be approximately a factor 2 larger for resonator B , which is not observed in the measurements. We therefore safely neglect this mechanism.

V. ESR SPECTRA SIMULATIONS

In this section, we assess whether the hydrostatic hyperfine shift can reproduce the measurement data by performing a full simulation of the extended ESR spectra of Fig. 4. The upper offset traces of Figs. 8(a) and 8(b) are the results of a numerical model incorporating the finite-element simulation of δB_1 and the hyperfine shift calculations [found by applying Eq. (4) to the strain simulations of Fig. 6]. For every pixel in the device where dopants are present, we use the predetermined $\Delta A(\epsilon)$ (with the

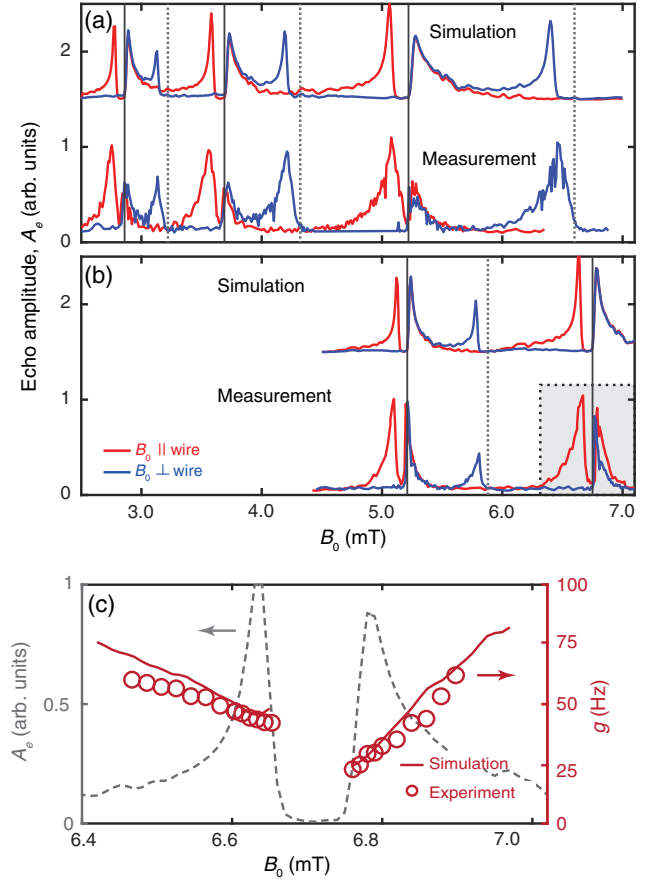


FIG. 8. (a) Rabi-levelled echo-detected field sweeps of transitions 1A–8A (resonator A). The bottom traces are the measured data from Fig. 4 (plotted again here for ease of comparison with theory), while the top traces are offset intentionally and are the results of our theoretical modeling. (b) Rabi-levelled echo-detected field sweeps (measurement and simulation) of transitions 1B–4B (resonator B). (c) The single spin-resonator coupling strength g as a function of the field B_0 , extracted from transition 4B [marked with a black dashed box in (b)]. The red open circles are derived from measurements of the Rabi frequency. Quantitative agreement is observed with the simulated data (the red solid line).

experimental value of K) and calculate the spin transition parameters by solving the modified Hamiltonian:

$$H/h = H_0/h + \Delta A(\epsilon)\mathbf{S} \cdot \mathbf{I}. \quad (5)$$

For each B_0 value, we calculate the spectral overlap of all allowed transitions ($\Delta m_F = \pm 1$ and $\Delta m_F = 0$) with the resonator and weight the resulting spectrum from each pixel with the corresponding donor concentration and the appropriate component of the magnetic-field vacuum fluctuations (Fig. 2), summing over all pixels to achieve the spectra in Figs. 8(a) and 8(b). We note that the donor doping profile used in this model [the red solid curve in Fig. 1(b)] is the output of a TCAD simulation (discussed in Sec. IV) that takes into account the ionization of donors in the depletion region of the Schottky junction formed between the aluminum wire and the silicon substrate. The simulation strikingly reproduces many features in the experimental data, including peak splittings, peak-height asymmetries, and field orientation ϕ dependence, without a single free parameter in the model.

Having successfully reproduced key features of the ESR spectra, we investigate whether our model can also capture the correlation of the magnetic-field vacuum fluctuations δB_1 and the spin-resonance frequency, as discussed in Sec. III. As noted previously, the Rabi frequency can be expressed in terms of the single spin-resonator coupling strength $g = \gamma_e M |\delta B_{1\perp}|$ and the mean intracavity photon number \bar{n} through the relation $\Omega_R = 2g\sqrt{\bar{n}}$. In the Rabi-levelled sweeps, Ω_R is held constant as we pass over the transitions. We extract g as a function of B_0 for transition 1B [identified with a black dashed box in Fig. 8(b)] by estimating \bar{n} at each field using the experimental input power and a calibration of the loss in our setup [13]. In Fig. 8(c), we plot the result of the experiment (the red open circles) overlaid on the simulated spectra (the gray dashed line). The data quantify the qualitative description offered earlier: the coupling strength (or, equivalently, the vacuum fluctuations δB_1) increases for the spins that are further detuned (those close to the edge of the wire) and reduces towards the center of the transition, reaching the lowest couplings at the inner edge of the high-field peak (the spins farthest from the wire). Next, we use our model to simulate the expected g versus B_0 dependence. The result [the red solid line in Fig. 8(c)] is an almost quantitative match to the experimental data.

VI. SUMMARY

In this paper, we discuss a range of mechanisms capable of altering the resonance frequencies of donors in micro- and nanoelectronic devices and find that strain resulting from differential thermal contraction plays a considerable part. We present a technique to study such strains in silicon devices through high-sensitivity orientation-dependent ESR spectroscopy. Our results are quantitatively reproduced by

considering the shift of the hyperfine interaction caused by the hydrostatic component of strain [48]. The resulting resonance frequency shifts of about 5 MHz for strains of approximately 10^{-4} contribute to an order-of-magnitude broadening of the ESR lines. While the measurements are performed on bismuth donors in silicon, similar effects are expected for the other group-V donors [48].

The level of agreement demonstrated between our model, which combines finite-element simulations and experimentally determined Hamiltonian parameters, and the measured data shows that it accurately captures the underlying physics. Remarkably, the simulation quantitatively reproduces the experimental results with no free parameters in the model. This analysis could be adapted to other device geometries and spin systems and may prove to be useful for spin-based device design. The results presented in this work have implications for QIP with donors and in hybrid systems such as superconducting quantum memories, which require a predictability of spin-resonance frequencies and the ability to engineer narrow spin linewidths.

The high sensitivity of the donor hyperfine interaction to hydrostatic strain could be used to create a sensitive local probe for strain in nanoelectronic devices. We estimate that, with typical intrinsic linewidths achieved for donors in isotopically enriched silicon of about 2 kHz [5], a single donor could be used to detect strains of order 10^{-7} . Such strain measurements could be integrated with other techniques for donor metrology [50] to provide valuable insight into the spatial variation of physical system parameters in nanoscale quantum devices. The large strain sensitivity also opens the prospect of driving spin resonance via mechanical resonators, or coupling donors to phonons in circuit quantum electrodynamics experiments.

ACKNOWLEDGMENTS

We thank B. Lovett and P. Mortemousque for the fruitful discussions. We acknowledge the support of the European Research Council under the European Community's Seventh Framework Programme (FP7) through Grant Agreements No. 615767 (CIRQUSS), No. 279781 (ASCENT), and No. 630070 (quRAM), the European Union's Horizon 2020 programme under Grant Agreement No. 688539 [51] and of the Agence Nationale de la Recherche (ANR) through the project QIPSE. J. J. L. M. was supported by the Royal Society. T. S. was supported by the U.S. Department of Energy under Contract No. DE-AC02-05CH11231. F. A. M. and A. M. were supported by Australian Research Council Discovery Project No. DP150101863. We acknowledge support from the Australian National Fabrication Facility.

APPENDIX A: SPIN-RESONANCE TRANSITIONS

The hyperfine interaction $\mathbf{AS} \cdot \mathbf{I}$ couples states in the $|m_S, m_I\rangle$ basis that differ in the electron and nuclear spin

projections such that $\Delta m_S = \pm 1$ and $\Delta m_I = \mp 1$. This mixing can be seen by rewriting the interaction as a product of the spin raising and lowering operators:

$$\begin{aligned} \mathbf{AS} \cdot \mathbf{I} &= A(S_X I_X + S_Y I_Y + S_Z I_Z) \\ &= A \left(S_Z I_Z + \frac{1}{2} [S_+ I_- + S_- I_+] \right). \end{aligned} \quad (\text{A1})$$

In the coupled $|F, m_F\rangle$ basis, these states therefore share the same value of $m_F = m_S + m_I$. In general, we can expand the $|F, m_F\rangle$ basis on the $|m_S, m_I\rangle$ basis as

$$|F_{\pm}, m_F\rangle = a_{m_F}^{\pm} \left| \pm \frac{1}{2}, m_F \mp \frac{1}{2} \right\rangle + b_{m_F}^{\pm} \left| \mp \frac{1}{2}, m_F \pm \frac{1}{2} \right\rangle, \quad (\text{A2})$$

where we use F_{\pm} to represent the higher or lower multiplet $F_{\pm} = I \pm S$ (i.e., $F_+ = 5$ and $F_- = 4$ for ^{209}Bi or the triplet and singlet states for ^{31}P). This expansion holds for all states except those with $m_F = \pm(I + S)$ (corresponding to $|m_S = \pm S, m_I = \pm I\rangle$), which remain unmixed. The mixing coefficients $a_{m_F}^{\pm}$ ($a_{m_F}^+ = a_{m_F}^-$) and $b_{m_F}^{\pm}$ ($b_{m_F}^+ = -b_{m_F}^-$) are determined by the value of m_F , the hyperfine interaction strength A and the external magnetic field B_0 (or, more precisely, the electron Zeeman energy relative to the hyperfine interaction) [9]. At high magnetic fields (where $E_z/h = \gamma_e B_0 \gg A$), $a_{m_F}^{\pm} \rightarrow 1$ and $b_{m_F}^{\pm} \rightarrow 0$, while, at low magnetic fields (where $\gamma_e B_0 \lesssim A$), strong mixing occurs.

1. S_X type

When operating in the “orthogonal mode” of spin resonance ($B_1 \perp B_0$), the B_1 field couples to the S_X and I_X spin operators. Electron spin-resonance transitions may be driven between $|F, m_F\rangle$ states that contain components of the uncoupled basis that differ by $\Delta m_S = \pm 1$, i.e., $|F_{\pm}, m_F\rangle \leftrightarrow |F_{\pm}, m_F - 1\rangle$ and $|F_{\pm}, m_F\rangle \leftrightarrow |F_{\mp}, m_F - 1\rangle$, as can be seen from Eq. (A2). The first two transitions, ($|F_+, m_F\rangle \leftrightarrow |F_+, m_F - 1\rangle$ and $|F_-, m_F\rangle \leftrightarrow |F_-, m_F - 1\rangle$), correspond to high-field NMR transitions (which become ESR allowed at low fields), while the third transition ($|F_+, m_F\rangle \leftrightarrow |F_-, m_F - 1\rangle$) is a high-field ESR transition, and the fourth ($|F_-, m_F\rangle \leftrightarrow |F_+, m_F - 1\rangle$) is completely forbidden at high fields—it corresponds to transitions where $\Delta m_S = \pm 1$ and $\Delta m_I = \mp 2$.

The transition matrix elements between these states are given by

$$\begin{aligned} \langle F_+, m_F | S_X + \delta I_X | F_+, m_F - 1 \rangle \\ = [a_{m_F}^+ b_{m_F-1}^+ + \delta(a_{m_F}^+ a_{m_F-1}^+ + b_{m_F}^+ b_{m_F-1}^+)]/2, \end{aligned} \quad (\text{A3a})$$

$$\begin{aligned} \langle F_-, m_F | S_X + \delta I_X | F_-, m_F - 1 \rangle \\ = [b_{m_F}^- a_{m_F-1}^- + \delta(a_{m_F}^- a_{m_F-1}^- + b_{m_F}^- b_{m_F-1}^-)]/2, \end{aligned} \quad (\text{A3b})$$

$$\begin{aligned} \langle F_+, m_F | S_X + \delta I_X | F_-, m_F - 1 \rangle \\ = [a_{m_F}^+ a_{m_F-1}^- + \delta(a_{m_F}^+ b_{m_F-1}^- + b_{m_F}^+ a_{m_F-1}^-)]/2, \end{aligned} \quad (\text{A3c})$$

$$\begin{aligned} \langle F_-, m_F | S_X + \delta I_X | F_+, m_F - 1 \rangle \\ = [b_{m_F}^- b_{m_F-1}^+ + \delta(b_{m_F}^- a_{m_F-1}^+ + a_{m_F}^- b_{m_F-1}^+)]/2, \end{aligned} \quad (\text{A3d})$$

where $\delta = \gamma_n/\gamma_e$ is the ratio of the nuclear and electron spin gyromagnetic ratios, which is typically on the order of 10^{-4} for group-V donors in silicon. At low and intermediate fields ($\gamma_e B_0 \lesssim A$), the first terms in the matrix elements of Eqs. (A3a)–(A3d) dominate over the components generated by the nuclear spin (those multiplied by δ). At high magnetic fields, the nuclear spin component of the matrix element is negligible for Eq. (A3c) but is the dominant term in Eqs. (A3a) and (A3b) (the high-field NMR transitions). It should be noted that, in general, the matrix elements above are nonzero at low fields, with the exception of identical particles ($S = I$ and $\delta = 1$) where the singlet state ($F = 0$) is ESR inactive. The singlet state becomes ESR active (for example, in the case of phosphorus $S = I = 1/2$) due to the differing gyromagnetic ratios of the electron and nuclear spins.

2. “ S_Z ” type

In the “parallel mode” of spin resonance ($B_1 \parallel B_0$), the B_1 field couples to the S_Z and I_Z spin operators. Electron spin-resonance transitions may be driven between $|F, m_F\rangle$ states that contain identical components of the uncoupled basis, i.e., $|F_{\pm}, m_F\rangle \leftrightarrow |F_{\mp}, m_F\rangle$ [see Eq. (A2)], corresponding to high-field flip-flop transitions ($\Delta m_S = \pm 1$ and $\Delta m_I = \mp 1$). The matrix element between these states is given by

$$\begin{aligned} \langle F_+, m_F | S_Z + \delta I_Z | F_-, m_F \rangle \\ = (a_{m_F}^+ b_{m_F}^- - a_{m_F}^- b_{m_F}^+)/2 \\ + \delta[a_{m_F}^+ b_{m_F}^- (m_F - 1/2) + a_{m_F}^- b_{m_F}^+ (m_F + 1/2)] \\ = -a_{m_F}^+ b_{m_F}^+ + \delta a_{m_F}^+ b_{m_F}^+, \end{aligned} \quad (\text{A4})$$

where we use the symmetry of the mixing coefficients ($a_{m_F}^+ = a_{m_F}^-$ and $b_{m_F}^+ = -b_{m_F}^-$) to arrive at the final form of Eq. (A4). Note that, for identical gyromagnetic ratios ($\delta = 1$), the components of the matrix element cancel exactly, and driving in the parallel mode is forbidden. Furthermore, at high fields (where $a_{m_F}^{\pm} \rightarrow 1$ and $b_{m_F}^{\pm} \rightarrow 0$), the matrix element becomes negligibly small. For the Si:Bi system ($\delta \approx 10^{-4}$) at low magnetic fields, the S_Z transitions are appreciable, comparable in strength to the S_X type.

APPENDIX B: PREDICTED ESR LINE SHAPE

Previous studies of the sample utilized in this work [24], performed using a bulk ESR spectrometer (i.e., without

the on-chip resonator) revealed a Gaussian line shape with a peak-to-peak width of $\sigma_B = 12 \mu\text{T}$ for the high-field $m_I = -1/2$ transition ($|4, -1\rangle \leftrightarrow |5, 0\rangle$ in the $|F, m_F\rangle$ basis), at a frequency of $\omega/2\pi = 9.53 \text{ GHz}$. This transition displays $df/dB = 0.6\gamma_e$, and thus an equivalent $\sigma_f = \sigma_B \times df/dB_0 = 200 \text{ kHz}$ broadening in the frequency domain. This value agrees well with other studies of bismuth-doped isotopically enriched silicon [10], where a linewidth of 270 kHz was measured and found to be constant in the frequency domain. For the $|4, -4\rangle \leftrightarrow |5, -5\rangle$ transition studied in this work (with $\omega/2\pi \approx 7.3 \text{ GHz}$), $df/dB_0 = -0.9\gamma_e$ (see Table I) and we expect $\sigma_B = \sigma_f/(df/dB_0) = 8 \mu\text{T}$, providing a FWHM of about $20 \mu\text{T}$. This width is substantially lower than the broadening we observe in our measurements using the on-chip microresonator, as depicted in Fig. 3.

APPENDIX C: MAGNETIC-FIELD INHOMOGENEITY

A magnetic-field inhomogeneity, for example, produced by a Meissner screening of the static magnetic field B_0 in the vicinity of the superconducting wire, is not expected to contribute to the splitting and broadening of the ESR peaks observed in our experiment (Figs. 3 and 4). We rule this mechanism out by comparing measurements of the first spin-resonance transition, $|4, -4\rangle \leftrightarrow |5, -5\rangle$ (see Table I), for each of the three resonators, A, B, and C (see Fig. 9). The width and the splitting of these peaks are of similar size for each resonator, despite the transition for resonator C ($B_0 = 9.29 \text{ mT}$, $df/dB_0 = -0.90\gamma_e$) occurring at twice the field of resonator B and 3 times the field of resonator A. A broadening resulting from an inhomogeneous magnetic field increases in proportion to the strength of the field.

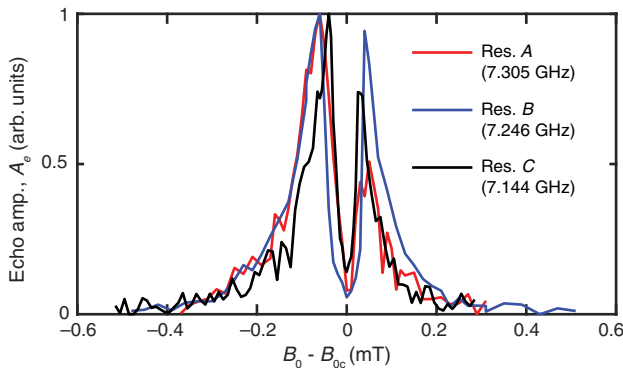


FIG. 9. Rabi-levelled echo-detected magnetic-field sweep (see Sec. III for measurement details) recorded for three resonators (frequencies are listed in the figure legend) over the first spin transition $|4, -4\rangle \leftrightarrow |5, -5\rangle$. The horizontal axis displays the difference with the transition center fields B_{0c} (listed in Table II). The transition frequency has a magnetic-field sensitivity of $df/dB_0 = -0.9\gamma_e$ for all three resonators.

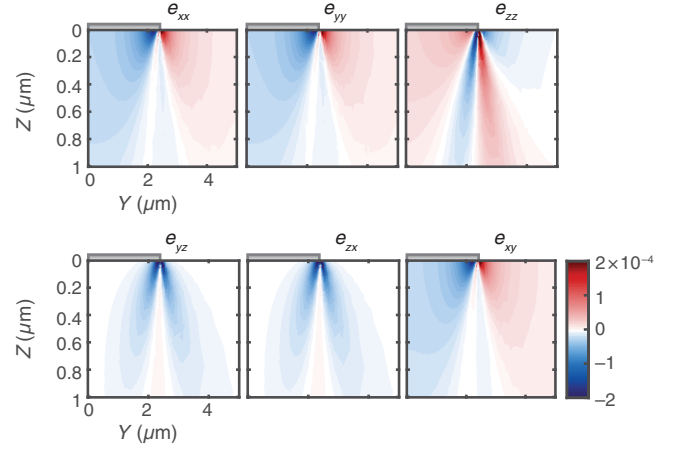


FIG. 10. Spatial dependence of the six independent components of strain in the silicon substrate. Donors are implanted up to a depth of about 300 nm. The strain tensor components are given in the cubic $[100]$ basis (xyz), while the cut through the device is such that $X||[110]$ and $Y||[\bar{1}10]$.

APPENDIX D: STRAIN TENSOR SIMULATION

We perform finite-element strain simulations of our device using the software package COMSOL Multiphysics. Our model consists of a 50-nm-thick, $5\text{-}\mu\text{m}$ -wide aluminum wire on a silicon substrate. We assume the aluminum to be strain-free upon deposition, and we simulate cooling the device to 20 mK using the temperature-dependent CTE of aluminum [40,41] and silicon [39], as well as the anisotropic stiffness coefficients for silicon [42]. The wire is constructed at a 45° angle to the x axis in the x - y plane (where $x||[100]$), such that it is aligned with the $[110]$ crystal axis. The difference between the CTEs of Si and Al produces device strains at low temperature. At each pixel in the device, we extract the six independent strain components in the $\langle 100 \rangle$ basis, which are plotted in Fig. 10.

- [1] Bruce E. Kane, A silicon-based nuclear spin quantum computer, *Nature (London)* **393**, 133 (1998).
- [2] Martin Fuechsle, Jill A. Miwa, Suddhasatta Mahapatra, Hoon Ryu, Sunhee Lee, Oliver Warschkow, Lloyd C. L. Hollenberg, Gerhard Klimeck, and Michelle Y. Simmons, A single-atom transistor, *Nat. Nanotechnol.* **7**, 242 (2012).
- [3] Jarryd J. Pla, Kuan Y. Tan, Juan P. Dehollain, Wee H. Lim, John J. L. Morton, Floris A. Zwanenburg, David N. Jamieson, Andrew S. Dzurak, and Andrea Morello, High-fidelity readout and control of a nuclear spin qubit in silicon, *Nature (London)* **496**, 334 (2013).
- [4] Lisa A. Tracy, Tzu-Ming Lu, N. C. Bishop, G. A. Ten Eyck, T. Pluym, J. R. Wendt, M. P. Lilly, and M. S. Carroll, Electron spin lifetime of a single antimony donor in silicon, *Appl. Phys. Lett.* **103**, 143115 (2013).
- [5] Juha T. Muhonen, Juan P. Dehollain, Arne Laucht, Fay E. Hudson, Takeharu Sekiguchi, Kohei M. Itoh, David N. Jamieson, Jeffrey C. McCallum, Andrew S. Dzurak, and

- Andrea Morello, Storing quantum information for 30 seconds in a nanoelectronic device, *Nat. Nanotechnol.* **9**, 986 (2014).
- [6] Solomon Freer, Stephanie Simmons, Arne Laucht, Juha T. Muhonen, Juan P. Dehollain, Rachpon Kalra, Fahd A. Mohiyaddin, Fay E. Hudson, Kohei M. Itoh, Jeffrey C. McCallum *et al.*, A single-atom quantum memory in silicon, *Quantum Sci. Technol.* **2**, 015009 (2017).
- [7] Alexei M. Tyryshkin, Shinichi Tojo, John J. L. Morton, Helge Riemann, Nikolai V. Abrosimov, Peter Becker, Hans-Joachim Pohl, Thomas Schenkel, Michael L. W. Thewalt, Kohei M. Itoh *et al.*, Electron spin coherence exceeding seconds in high-purity silicon, *Nat. Mater.* **11**, 143 (2012).
- [8] Kamyar Saeedi, Stephanie Simmons, Jeff Z. Salvail, Phillip Dluhy, Helge Riemann, Nikolai V. Abrosimov, Peter Becker, Hans-Joachim Pohl, John J. L. Morton, and Mike L. W. Thewalt, Room-temperature quantum bit storage exceeding 39 minutes using ionized donors in silicon-28, *Science* **342**, 830 (2013).
- [9] M. H. Mohammady, G. W. Morley, and T. S. Monteiro, Bismuth Qubits in Silicon: The Role of EPR Cancellation Resonances, *Phys. Rev. Lett.* **105**, 067602 (2010).
- [10] Gary Wolfowicz, Alexei M. Tyryshkin, Richard E. George, Helge Riemann, Nikolai V. Abrosimov, Peter Becker, Hans-Joachim Pohl, Mike L. W. Thewalt, Stephen A. Lyon, and John J. L. Morton, Atomic clock transitions in silicon-based spin qubits, *Nat. Nanotechnol.* **8**, 561 (2013).
- [11] T. Yasukawa, A. J. Sigillito, B. C. Rose, A. M. Tyryshkin, and S. A. Lyon, Addressing spin transitions on ^{209}Bi donors in silicon using circularly polarized microwaves, *Phys. Rev. B* **93**, 121306 (2016).
- [12] A. Bienfait, J. J. Pla, Y. Kubo, M. Stern, X. Zhou, C. C. Lo, C. D. Weis, T. Schenkel, M. L. W. Thewalt, D. Vion *et al.*, Reaching the quantum limit of sensitivity in electron spin resonance, *Nat. Nanotechnol.* **11**, 253 (2016).
- [13] A. Bienfait, J. J. Pla, Y. Kubo, X. Zhou, M. Stern, C. C. Lo, C. D. Weis, T. Schenkel, D. Vion, D. Esteve *et al.*, Controlling spin relaxation with a cavity, *Nature (London)* **531**, 74 (2016).
- [14] J. H. Wesenberg, A. Ardavan, G. A. D. Briggs, J. J. L. Morton, R. J. Schoelkopf, D. I. Schuster, and K. Mølmer, Quantum Computing with an Electron Spin Ensemble, *Phys. Rev. Lett.* **103**, 070502 (2009).
- [15] Y. Kubo, C. Grezes, A. Dewes, T. Umeda, J. Isoya, H. Sumiya, N. Morishita, H. Abe, S. Onoda, T. Ohshima, V. Jacques, A. Dréau, J. F. Roch, I. Diniz, A. Auffeves, D. Vion, D. Esteve, and P. Bertet, Hybrid Quantum Circuit with a Superconducting Qubit Coupled to a Spin Ensemble, *Phys. Rev. Lett.* **107**, 220501 (2011).
- [16] Brian Julsgaard, Cécile Grezes, Patrice Bertet, and Klaus Mølmer, Quantum Memory for Microwave Photons in an Inhomogeneously Broadened Spin Ensemble, *Phys. Rev. Lett.* **110**, 250503 (2013).
- [17] C. Grezes, B. Julsgaard, Y. Kubo, M. Stern, T. Umeda, J. Isoya, H. Sumiya, H. Abe, S. Onoda, T. Ohshima, V. Jacques, J. Esteve, D. Vion, D. Esteve, K. Mølmer, and P. Bertet, Multimode Storage and Retrieval of Microwave Fields in a Spin Ensemble, *Phys. Rev. X* **4**, 021049 (2014).
- [18] Susan J. Angus, Andrew J. Ferguson, Andrew S. Dzurak, and Robert G. Clark, Gate-defined quantum dots in intrinsic silicon, *Nano Lett.* **7**, 2051 (2007).
- [19] Jarryd J. Pla, Kuan Y. Tan, Juan P. Dehollain, Wee H. Lim, John J. L. Morton, David N. Jamieson, Andrew S. Dzurak, and Andrea Morello, A single-atom electron spin qubit in silicon, *Nature (London)* **489**, 541 (2012).
- [20] Arne Laucht, Juha T. Muhonen, Fahd A. Mohiyaddin, Rachpon Kalra, Juan P. Dehollain, Solomon Freer, Fay E. Hudson, Menno Veldhorst, Rajib Rahman, Gerhard Klimeck *et al.*, Electrically controlling single-spin qubits in a continuous microwave field, *Sci. Adv.* **1**, e1500022 (2015).
- [21] Lisa A. Tracy, Dwight R. Luhman, Stephen M. Carr, Nathaniel C. Bishop, Gregory A. Ten Eyck, Tammy Pluym, Joel R. Wendt, Michael P. Lilly, and Malcolm S. Carroll, Single shot spin readout using a cryogenic high-electron-mobility transistor amplifier at sub-kelvin temperatures, *Appl. Phys. Lett.* **108**, 063101 (2016).
- [22] C. C. Lo, M. Urdampilleta, P. Ross, M. F. Gonzalez-Zalba, J. Mansir, S. A. Lyon, M. L. W. Thewalt, and J. J. L. Morton, Hybrid optical-electrical detection of donor electron spins with bound excitons in silicon, *Nat. Mater.* **14**, 490 (2015).
- [23] Ted Thorbeck and Neil M. Zimmerman, Formation of strain-induced quantum dots in gated semiconductor nanostructures, *AIP Adv.* **5**, 087107 (2015).
- [24] C. D. Weis, C. C. Lo, V. Lang, A. M. Tyryshkin, R. E. George, K. M. Yu, J. Bokor, S. A. Lyon, J. J. L. Morton, and T. Schenkel, Electrical activation and electron spin resonance measurements of implanted bismuth in isotopically enriched silicon-28, *Appl. Phys. Lett.* **100**, 172104 (2012).
- [25] Ted Van Duzer and Charles W. Turner, *Principles of Superconductive Devices and Circuits* (Prentice-Hall, Englewood Cliffs, NJ, 1999).
- [26] Ernst Helmut Brandt, Thin Ohmic or superconducting strip with an applied ac electric current, *Phys. Rev. B* **73**, 092511 (2006).
- [27] I. S. Wisby, S. E. de Graaf, R. Gwilliam, A. Adamyan, S. E. Kubatkin, P. J. Meeson, A. Ya. Tzalenchuk, and T. Lindström, Angle-Dependent Microresonator ESR Characterization of Locally Doped $\text{Gd}^{3+}:\text{Al}_2\text{O}_3$, *Phys. Rev. Applied* **6**, 024021 (2016).
- [28] A. Bienfait, P. Campagne-Ibarcq, A. H. Küllerich, X. Zhou, S. Probst, J. J. Pla, T. Schenkel, D. Vion, D. Esteve, J. J. L. Morton, K. Moelmer, and P. Bertet, Magnetic Resonance with Squeezed Microwaves, *Phys. Rev. X* **7**, 041011 (2017).
- [29] S. Probst, A. Bienfait, P. Campagne-Ibarcq, J. J. Pla, B. Albanese, J. F. Da Silva Barbosa, T. Schenkel, D. Vion, Daniel Esteve, Klaus Mølmer *et al.*, Inductive-detection electron-spin resonance spectroscopy with 65 spins/Hz sensitivity, *Appl. Phys. Lett.* **111**, 202604 (2017).
- [30] E. Hahn, Spin echoes, *Phys. Rev.* **80**, 580 (1950).
- [31] E. H. Rhoderick, Metal-semiconductor contacts, *IEE Proc., Part I: Solid-State Electron Devices* **129**, 1 (1982).
- [32] Giuseppe Pica, Gary Wolfowicz, Matias Urdampilleta, Mike L. W. Thewalt, Helge Riemann, Nikolai V. Abrosimov, Peter Becker, Hans-Joachim Pohl, John J. L. Morton, R. N. Bhatt *et al.*, Hyperfine stark effect of shallow donors in silicon, *Phys. Rev. B* **90**, 195204 (2014).

- [33] Devin Underwood, APS March Meeting 2017, abstract id. F52.008, <http://adsabs.harvard.edu/abs/2017APS..MARF52008U>.
- [34] David P. Franke, Florian M. Hrubesch, Markus Künzl, Hans-Werner Becker, Kohei M. Itoh, Martin Stutzmann, Felix Hoehne, Lukas Dreher, and Martin S. Brandt, Interaction of Strain and Nuclear Spins in Silicon: Quadrupolar Effects on Ionized Donors, *Phys. Rev. Lett.* **115**, 057601 (2015).
- [35] David P. Franke, Moritz P. D. Pflüger, Pierre-André Mortemousque, Kohei M. Itoh, and Martin S. Brandt, Quadrupolar effects on nuclear spins of neutral arsenic donors in silicon, *Phys. Rev. B* **93**, 161303 (2016).
- [36] Lukas Dreher, Timon A. Hilker, Andreas Brandlmaier, Sebastian T. B. Goennenwein, Hans Huebl, Martin Stutzmann, and Martin S. Brandt, Electroelastic Hyperfine Tuning of Phosphorus Donors in Silicon, *Phys. Rev. Lett.* **106**, 037601 (2011).
- [37] E. Eiper, R. Resel, C. Eisenmenger-Sittner, M. Hafok, and J. Keckes, Thermally-induced stresses in thin aluminum layers grown on silicon, *Powder Diffr.* **19**, 74 (2004).
- [38] Marc J. Madou, *Fundamentals of Microfabrication: The Science of Miniaturization* (CRC Press, Boca Raton, 2002).
- [39] C. A. Swenson, Recommended values for the thermal expansivity of silicon from 0 to 1000 K, *J. Phys. Chem. Ref. Data* **12**, 179 (1983).
- [40] F. C. Nix and D. MacNair, The thermal expansion of pure metals: Copper, gold, aluminum, nickel, and iron, *Phys. Rev.* **60**, 597 (1941).
- [41] Weileun Fang and Chun-Yen Lo, On the thermal expansion coefficients of thin films, *Sens. Actuators A* **84**, 310 (2000).
- [42] Matthew A. Hopcroft, William D. Nix, and Thomas W. Kenny, What is the Young's modulus of silicon?, *J. Microelectromech. Syst.* **19**, 229 (2010).
- [43] P. A. Mortemousque, S. Rosenius, G. Pica, D. P. Franke, T. Sekiguchi, A. Truong, M. P. Vlasenko, L. S. Vlasenko, M. S. Brandt, R. G. Elliman *et al.*, Quadrupole shift of nuclear magnetic resonance of donors in silicon at low magnetic field, *Nanotechnology* **27**, 494001 (2016).
- [44] Elton N. Kaufmann and Reiner J. Vianden, The electric field gradient in noncubic metals, *Rev. Mod. Phys.* **51**, 161 (1979).
- [45] Tsuneya Ando, Alan B. Fowler, and Frank Stern, Electronic properties of two-dimensional systems, *Rev. Mod. Phys.* **54**, 437 (1982).
- [46] W. Kohn and J. M. Luttinger, Theory of donor states in silicon, *Phys. Rev.* **98**, 915 (1955).
- [47] D. K. Wilson and G. Feher, Electron spin resonance experiments on donors in silicon. III. Investigation of excited states by the application of uniaxial stress and their importance in relaxation processes, *Phys. Rev.* **124**, 1068 (1961).
- [48] John Mansir, Pierandrea Conti, Zaiping Zeng, Jarryd J. Pla, Patrice Bertet, Yann-Michel Niquet, and John J. L. Morton, Linear Hyperfine Tuning of Donor Spins in Silicon Using Hydrostatic Strain, [arXiv:1710.00723](https://arxiv.org/abs/1710.00723) [*Phys. Rev. Lett.* (to be published)].
- [49] Forrest R. Bradbury, Alexei M. Tyryshkin, Guillaume Sabouret, Jeff Bokor, Thomas Schenkel, and Stephen A. Lyon, Stark Tuning of Donor Electron Spins in Silicon, *Phys. Rev. Lett.* **97**, 176404 (2006).
- [50] Fahd A. Mohiyaddin, Rajib Rahman, Rachpon Kalra, Gerhard Klimeck, Lloyd C. L. Hollenberg, Jarryd J. Pla, Andrew S. Dzurak, and Andrea Morello, Noninvasive spatial metrology of single-atom devices, *Nano Lett.* **13**, 1903 (2013).
- [51] <http://mos-quito.eu>.